Applied Energy 225 (2018) 746–754

Contents lists available at ScienceDirect

Applied Energy

journal homepage: www.elsevier.com/locate/apenergy

Screen-printed radial structure micro radioisotope thermoelectric generator

Zicheng Yuan[a], Xiaobin Tang[a,b,*], Zhiheng Xu[a], Junqin Li[a], Wang Chen[a], Kai Liu[a], Yunpeng Liu[a,b], Zhengrong Zhang[a]

[a] Department of Nuclear Science and Engineering, Nanjing University of Aeronautics and Astronautics, Nanjing 211106, China
[b] Jiangsu Key Laboratory of Material and Technology for Energy Conversion, Nanjing 211106, China

HIGHLIGHTS

- The prototype of the micro radioisotope thermoelectric generator was fabricated by screen printing.
- The matching scheme of the thermoelectric leg material is compared.
- Three types of radioactive isotopes were considered for experiments.
- 5 pairs of thermoelectric legs has an V_{oc} of 68.41 mV, I_{sc} of 328.96 μA and an P_{max} of 5.81 μW.

GRAPHICAL ABSTRACT

A new solution for micro-isotope power supply is proposed. The prototype of the radial structure micro RTG was fabricated by the screen printing. Curing temperature was designed for optimal material properties. The prototype's electrical performance was tested and evaluated. This type of energy harvester may provide a new idea for energy development in the future space exploration missions. It can be used not only in micro RTG but also in lightweight applications.

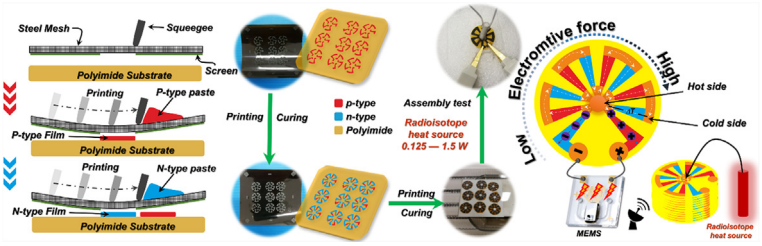

ARTICLE INFO

Keywords:
Radioisotope thermoelectric generator
Screen printing
$(BiSb)_2(TeSe)_3$
Sensor power supply
Radial structure

ABSTRACT

The micro radioisotope thermoelectric generator can be invoked as a long-life power supply in low-power device applications. Improving the current, voltage and power of power sensors by enhancing the properties of thermoelectric material composites matters in low-power device applications. The micro radioisotope thermoelectric generator driven by the temperature difference between radial thermoelectric legs printed on polyimide substrate and the loaded central heat source is reported in this study. The electrical conductivity of n-type $Bi_2Te_{2.7}Se_{0.3}$, p-type $Bi_{0.5}Sb_{1.5}Te_3$, and p-type Sb_2Te_3 radial thermoelectric legs are 24.57–165.8 $S{\cdot}cm^{-1}$, with Seebeck coefficients of −176.6, 223.3 and 139.7 $\mu V{\cdot}K^{-1}$ respectively. Thermoelectric legs are prepared by screen printing with a paste consisting of epoxy resin and BiTe-based powders. The generator has five couples of radial thermoelectric legs, and their material properties are optimized through selecting the preliminary curing temperature. The electrical conductivity of n-type $Bi_2Te_{2.7}Se_{0.3}$, p-type $Bi_{0.5}Sb_{1.5}Te_3$, and p-type Sb_2Te_3 thermoelectric legs are 24.57–165.8 $S{\cdot}cm^{-1}$, with Seebeck coefficients of −176.6, 223.3 and 139.7 $\mu V{\cdot}K^{-1}$ respectively. When loaded with 1.5 W isotope heat sources, the prototype generator would generate an open-circuit voltage of 68.41 mV, a short-circuit current of 329.0 μA, and an output power of 5.81 μW at 39.20 mV. Stacking and series-parallel can harvest considerable energy.

* Corresponding author at: Department of Nuclear Science and Engineering, Nanjing University of Aeronautics and Astronautics, Nanjing 211106, China.
E-mail address: tangxiaobin@nuaa.edu.cn (X. Tang).

https://doi.org/10.1016/j.apenergy.2018.05.073
Received 12 February 2018; Received in revised form 7 May 2018; Accepted 20 May 2018

Nomenclature

σ	electrical conductivity ($S{\cdot}m^{-1}$)
n	carrier concentration (cm^{-3})
e	quantity of electric charge
μ	carrier mobility ($cm^2{\cdot}V^{-1}{\cdot}s^{-1}$)
S	seebeck coefficient ($\mu V{\cdot}K^{-1}$)
k_B	Boltzmann constant
h	Planck's constant
m^*	effective mass of the carrier
T	absolute temperature (K)
PF	power fator ($W{\cdot}m^{-1}{\cdot}K^{-2}$)
α	seebeck coefficient ($\mu V{\cdot}K^{-1}$)
ΔV	voltage difference (V)
V_c	cold-side voltage (V)
V_h	hot-side voltage (V)
ΔT	temperature difference (K)
T_h	temperature of hot end (K)
T_c	temperature of cold end (K)
V_{oc}	open-circuit voltage (V)
I_{sc}	short-circuit current (A)
N	the number of thermoelectric legs
α_p	p-type Seebeck coefficient ($\mu V{\cdot}K^{-1}$)
α_n	n-type Seebeck coefficient ($\mu V{\cdot}K^{-1}$)
P_{th}	radioisotope thermal power (W)
P_{max}	maximum output power (W)
R_{int}	internal resistance (Ω)
R_{load}	load resistance (Ω)
TE	thermoelectric

1. Introduction

The radioisotope thermoelectric generator (RTG) converting radioisotope heat into electric power by thermoelectric (TE) material without moving parts has numerous advantages, such as high reliability, long lifetime, and minimal environmental impact [1–4]. The increasing number of small spacecraft and studies on potential scientific applications indicates the need for RTG application at low power levels. Micro RTGs (MRTGs) mainly lend themselves to small, long-life power devices. Moreover, MRTG can provide stable long-term power output for low-power sensing devices when carrying out deep space missions [5]. The application range of miniature scientific instruments, for example, the small long-life meteorological/seismological stations distributed across planetary surfaces, subsurface probes, deep space microspacecrafts and sub-satellites, is very likely to extend due to such power supply [4]. However, the minor temperature difference, low efficiency and insufficient reliability of the miniaturized RTG currently limit its application in space missions. As regard to the output performance problem of RTG, a novel micro RTG is designed to improve the above shortcomings in this paper.

TE modules in RTG can convert the energy between heat energy and electric energy directly, diversely applied in harvesting and sensing energy at the same time [6,7]. The optimization of structure and material is important to the properties of thermoelectric devices [8]. Whalen et al. have used 11 pairs of 215 μm-thick Bi_2Te_3 in the design of a wheel spoke thermocouple, and optimized the thermopile through cutting the thermoelectric material by four equal parts. [9]. Menon et al. have stacked 15p–n radial TE couples in series, and further obtained the voltage and power increasing in linear along with TE [10,11]. The application of block and thick-film devices with this structure has been reported in previous work. The number of elements and power in a given area needs to be balanced [12,13]. Semiconductor alloy materials based on Bi_2Te_3 have the brittleness characteristics [14]. In particular, the devices of long-life micro radioisotope of TEGs based on printed thick film BiTe requires a high degree of mechanical stability and flexibility. Physical cutting methods can no longer meet the thin film requirements for fabricating devices with radial structures. Thus methods of molding the thick film TE material need to be changed. As for the 2D additive manufacturing method, the screen printing has the advantages of low cost, rapid prototyping and mass manufacturing. Son and Cho et al. have applied the screen printing method to produce high-performance thermoelectric generator by using all-inorganic and hybrid viscoelastic inks in recent years [15–17]. A large number of thermocouples can be manufactured rapidly by screen printing, able to provide high electric power, which is indeed a developed and appropriate program [18,19]. RTG's reliability is similar to the requirements on flexibility and output performance of a wearable thermoelectric device [20–22]. Polymer thermoelectric composite materials are very attractive owing to its low cost, flexibility and high power density [23]. Madan et al. have reported a flexible thermoelectric generator of polymer thermoelectric composite, used in flexible and high output practical wireless sensor networks [24]. Gima et al. have reported 50-couple screen printed $Bi_2Te_3/Bi_{0.5}Sb_{1.5}Te_3$-epoxy annular thermoelectric generators, used in ultra-low-power sensors, with the average power of 0.068 nW at a 20 K temperature gradient, 26nA and 2.6 mV [25]. In this study, we have investigated the TE properties of MRTG composite materials. In addition, a new manufacturing process is optimized, and the properties of the composite semiconductor material are explored. Furthermore, a prototype with five pairs of TE legs, diameter of 1.5 cm, and an area of 1.77 cm^2 is prepared. It is tested by loading a radioisotope heat source. The output performance of the MRTG is further evaluated.

Moreover, it will improve the energy conversion efficiency by fabricating planar array and space stack thermoelectric devices. Thus, the thermoelectric device technology deserves to be promoted because of the simple heat treatment process, equipment manufacturing process, heat treatment conditions, and the whole process posing no harm to the environment. The use of new thermoelectric device manufacturing technology is not limited to micro RTG. Various lightweight devices, such as low-cost flexible wearable generators, solar thermal generators and pipe powering wireless sensors are also welcomed [20,26].

2. Materials and methods

2.1. Bi_2Te_3–epoxy TE paste synthesis

TE bulk ingots are prepared as TE powder (i.e., p-type $Bi_{0.5}Sb_{1.5}Te_3$, Sb_2Te_3 and n-type $Bi_2Te_{2.7}Se_{0.3}$) through airflow milling. The powder needs to be sieved through a 325 mesh screen before use. The polymer binder is an epoxy system formulated by the polypropylene glycol diglycidyl ether epoxy resin (Sigma-Aldrich) and the methylhexahydrophthalic anhydride (Sigma-Aldrich). Among them, the equivalent weight ratio of epoxy and hardener is 1:0.85. Furthermore, use the 1-Cyanoethyl-2-ethyl-4-methylimidazole (0.5 wt%; Shikoku Chemicals) as the catalyst in the system.

The TE powder occupies 45–50 vol% of and paste (Fig. S1). Add the butyl acetate (Sigma-Aldrich) to the resin blend to reduce the viscosity of the ink as a nonreactive diluent. Furthermore, the low percentages of organic solvents are used to extend the shelf life of the epoxy system so as to adjust the viscosity for printing, and the epoxy system is selected in this work owing to its low viscosity and extended pot life. Use the planetary mixer to mix the powder and solvent cement uniformly. Mix the turbid liquid system at 1000 rpm for 3 min, being held for 1 min, and mix it again at 1800 rpm for 3 min.

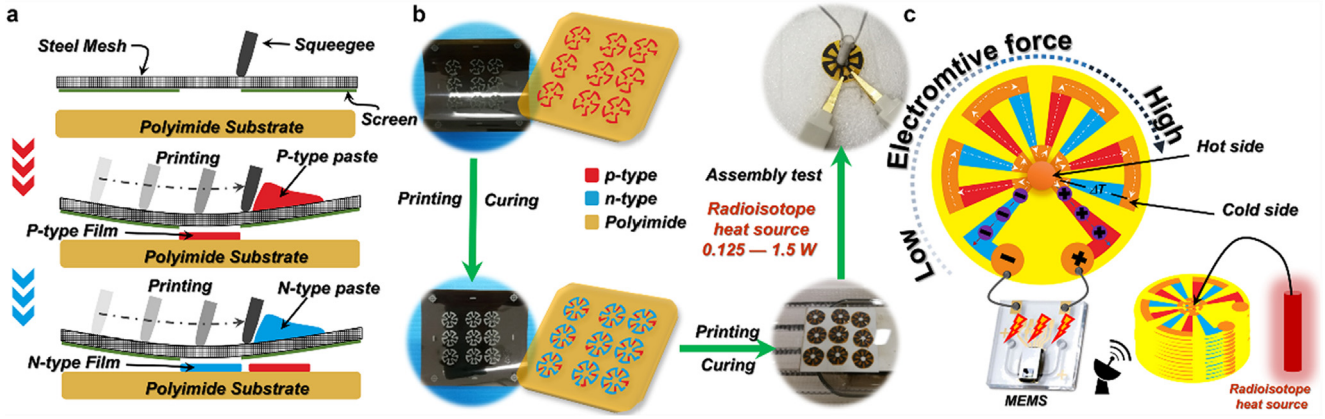

Fig. 1. Formation of TE thick films (a and b) and concept of MRTG (c).

Table 1
Comparison of crucial radioisotope heat source material properties.

Parameters	$^{238}PuO_2$	$^{90}SrTiO_3$	$^{241}AmO_2$
Half-life of isotope ($T_{1/2}$, year)	87.7	28.9	432.7
Specific activity (Ci/g)	15	133	3.43
Power per activity (μW/Ci)	32000.0	6665.92	32362.0
Density (g/cm^3)	11.5	5.11	13.67
Initial volumetric power density (W/cm^3)	5.52	4.54	1.52
Heat source thermal power (W)	1.564	1.287	0.431

2.2. Device structure fabrication by screen printing

The steel mesh aperture is 200 mesh. The square samples are formed through successively curing the printed p-type, n-type, and electrode on the polyimide film substrate at 90 °C for 2 h. Then, cure the square samples at various temperatures (i.e., 150 °C, 200 °C, 250 °C, 300 °C, and 350 °C) for 6 h in N_2 atmosphere tube furnace to prevent oxidation. Further, print the shape of thermoelectric legs onto a fixed transparent substrate for printing visual alignment. TE legs used for device fabrication need to be cured twice. Moreover, fix the polyimide film substrate used for visual alignment before printing TE legs on a plate with preprinted patterns. Then, cure the p-type TE legs at 90 °C for 2 h and 300 °C for 6 h after being printed. After that, cut the samples used for device fabrication into round slices, and punch a hole at the center. Finally, the TE legs are cured at 90 °C for 2 h, and then 300 °C for 6 h.

The procedure usually involves printing, drying, printing, and curing. However, the thermoelectric legs from the second printing is incomplete owing to the stickiness of paste, which causes strong resistance and even the non-conductivity [25]. Curing is thus divided into two steps: materials are cured after the first printing; materials do not adhere to the screen after the second printing, thereby the internal resistance of the generator is reduced.

As shown in Fig. 1c, the prototype device comprises several thermocouples, among which, one thermocouple includes one n-type leg and one p-type leg. This radial distribution structure enables thermal energy to flux from the center of the heat source in a radial pattern, and thermal flux to flow from inside to outside through the thermocouples. Red and blue elements in the figure represent p-type and n-type TE semiconductors respectively, and the temperature difference causes hole carriers and electron carriers in the semiconductor to diffuse outside (cold side) from the center (hot end). The potential vector presents from inside to outside in p-type, which is opposite to that in n-type.

2.3. Radioisotope heat source

By the power density and mission time, the output of three typical radioisotope heat sources is compared. According to the parameters of the isotope material, as listed in Table 1 [27], the heat source thermal power could be calculated, then the simulation thermal power value of the surrogate heat source is obtained. The heat source power cannot exceed the power limit arising from the volume and power density. Thus, setting the thermal power as 0.125, 0.25, 0.5, 0.75, 1, and 1.5 W may act as a reference for heat sources with different variety or purity in the experiment 2.3.

2.4. Characterization of TE thick film performance

Seebeck coefficient measurements of the printed TE films are conducted using a custom testing device. The Seebeck coefficient is determined according to the voltage difference (ΔV) and temperature difference (ΔT) curves obtained through using a multimeter (Agilent 34970A Data Acquisition with 34901A 20 Channel Multiplexer, Agilent; Fig. S2). Electrical conductivity, carrier concentration, and mobility are obtained by using a Hall measurement system (HT-50, HONOR TOP). The magnetic flux density is 0.5 T, and the electrical current is 15 mA. X-ray diffraction (XRD) patterns are obtained through using a Cu Kα X-ray source at 40 kV and 40 mA. Morphologies of the materials are imaged through using a Quanta 650 FEG scanning electron microscope (SEM; Thermo Fisher Scientific, USA) operating at 15 kV. During SEM measurements, EDS (X-act SDD detector, Oxford Instruments, UK) data are obtained so as to analyze the chemical elements.

The square standard samples (70 μm × 20 mm × 20 mm (Fig. 2a)) are used to test the electrical conductivity and conduct the Seebeck coefficient measurements.

2.5. Measurement of MRTG application

The heat source rod is loaded vertically into the hole, which is at the center of the radial TE leg samples. The lower part of the heat source bar is covered with foamed plastic to reduce heat loss. A resistive joule thermal surrogate is used in the MRTG to simulate a radioactive fuel pellet for experimental research (see Fig. 6). The power for the heat source rods is provided by a programmable linear DC power supply (DP832A, RIGOL Technologies Inc.). The power range of 0–1.5 W represents the three heat source columns, with the corresponding rule shown in Table 2. J-type thermocouples are placed on the hot and cold sides of the prototype so as to monitor ΔT across the device. The MRTG

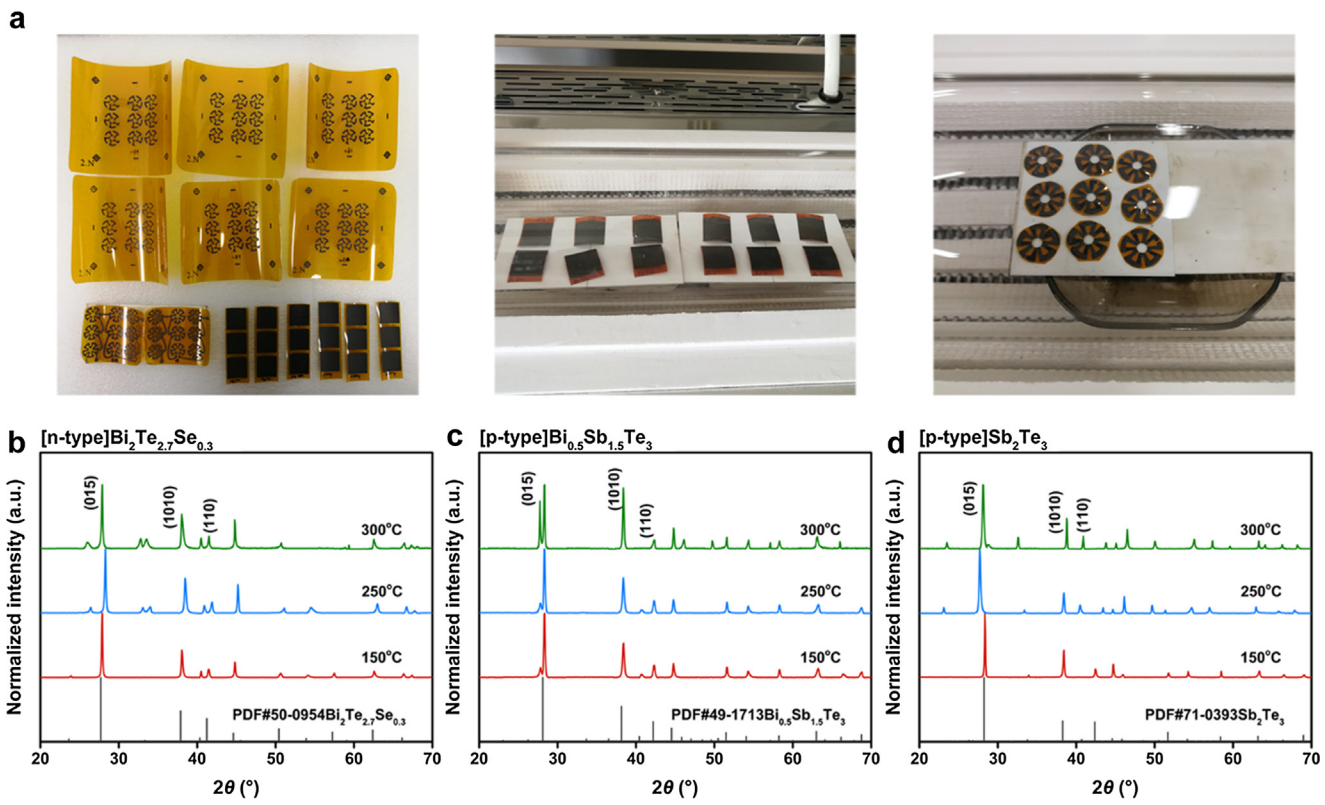

Fig. 2. (a) TE paste printed in various shapes with radial TE legs and square samples. X-ray diffraction (XRD) patterns of screen-printed (b) n-type $Bi_2Te_{2.7}Se_{0.3}$, (c) p-type $Bi_{0.5}Sb_{1.5}Te_3$, and (d) p-type Sb_2Te_3 samples with different curing temperatures. Insets show that the XRD pattern is indexed to the corresponding JCPDF.

is connected to a parameter analyzer (Keithley 4200-SCS). *I–V* characteristics are measured using software KTEI (Keithley Test Environment Interactive).

3. Result and discussion

3.1. Material properties of screen-printed TE thick films

Fig. 2b-d shows the XRD spectra of the n-type $Bi_2Te_{2.7}Se_{0.3}$, p-type $Bi_{0.5}Sb_{1.5}Te_3$, and p-type Sb_2Te_3 samples, prepared by increasing the curing temperature from 150 °C to 300 °C. The XRD peaks of the samples can be indexed to the corresponding JCPDF crystal samples (i.e., JCPDF Nos. 50-0954, 49-1713, and 71-0393). Element types and content are consistent with TE powder and epoxy resin (Fig. S3).

Fig. 3 shows the function relationship of curing temperature and the TE properties of composite films measured at room temperature. The figure shows the carrier concentration of the three TE composite films. The carrier concentration of $Bi_2Te_{2.7}Se_{0.3}$ and Sb_2Te_3 increases along with the increased temperature, and the opposite for $Bi_{0.5}Sb_{1.5}Te_3$ after the temperature is more than 250 °C. The Seebeck coefficient of a similar metal-doped degenerate semiconductor may be affected by the carrier concentration. Thus these properties will affect the TE properties of the material.

$$\sigma = ne\mu \tag{1}$$

$$S = \frac{8\pi^2 k_B^2}{3eh^2} m^* T \left(\frac{\pi}{3n}\right)^{2/3} \tag{2}$$

The relationship between Seebeck coefficient and power factor are shown in TE characteristics of (a and b) Bi2Te2.7Se0.3, (c and d) Bi0.5Sb1.5Te3, and (e and f) Sb2Te3 thick films as a function of curing temperature. All samples are cured for 6 h. Fig. 3b, d, and f, and their values are obtained according to the following equation:

$$\Delta V = V_c - V_h, \tag{3}$$

$$\Delta T = T_h - T_c, \tag{4}$$

$$\alpha = \frac{dV}{dT} = \lim_{\Delta T \to 0} \frac{\Delta V}{\Delta T}, \tag{5}$$

$$PF = \alpha^2 \sigma. \tag{6}$$

The conductivity will be determined by the carrier concentration and mobility along with the change in curing temperature [28–30]. Hall effect tests reflect that mobility increases more slowly than carrier concentration. In the low-temperature curing process, the contribution of carrier concentration to conductivity is significant. The variation of the Seebeck coefficient is different from that of high-temperature sintering, and a trend of monotonic decrease with the carrier concentration is not observed. These resin composite TE materials may have lost the performance of degenerate semiconductors. Because $Bi_{0.5}Sb_{1.5}Te_3$ has a high melting point and low electrical conductivity, the conductivity of the composite material system is lower than that of the others though its Seebeck voltage is higher than that of the other (Fig. 4a). Property variation of Sb_2Te_3 in this study is consistent with that in similar research [31,32]. In fact, the samples cured with temperature above 300 °C have a high fragmentation rate after incinerating the cured epoxy resin. Given the power factor (Fig. 4b), p-type Sb_2Te_3 and n-type $Bi_2Te_{2.7}Se_{0.3}$ at 300 °C should be the preferred solution.

The slope of the ΔT–ΔV function (Fig. 4a) represented the values of the Seebeck coefficients of n-type $Bi_2Te_{2.7}Se_{0.3}$, p-type $Bi_{0.5}Sb_{1.5}Te_3$, and p-type Sb_2Te_3 (cured at 300 °C) of −176.6, 223.3, and 139.7 $\mu V K^{-1}$, respectively. The square standard samples (70 μm × 20 mm × 20 mm) are cured at 300 °C for 6 h after being cured at 90 °C.

3.2. TE legs case of MRTG

A comparison of the experimental output performance of two combinations is shown in Fig. 5. The n-type TE legs amid the two

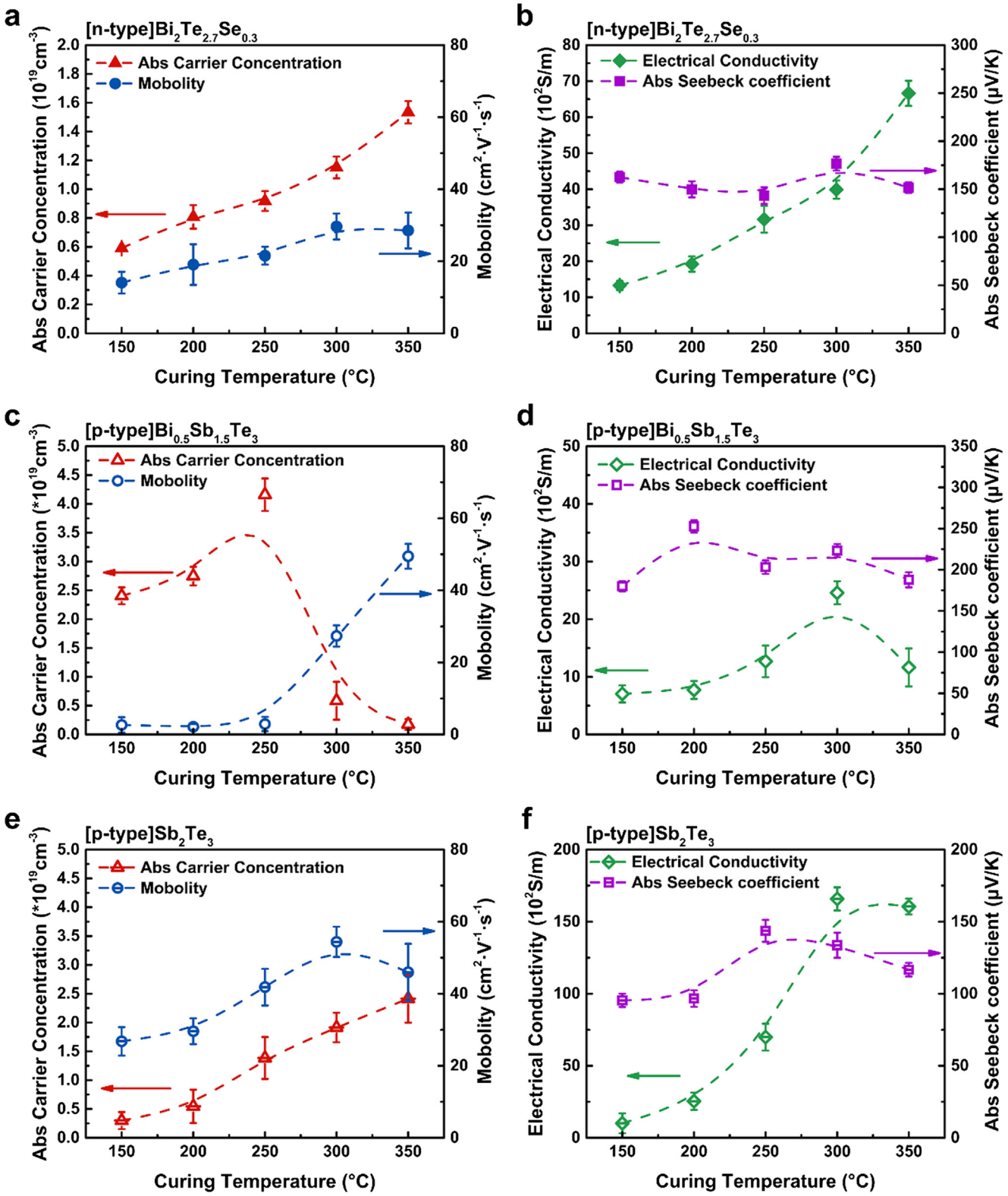

Fig. 3. TE characteristics of (a and b) $Bi_2Te_{2.7}Se_{0.3}$, (c and d) $Bi_{0.5}Sb_{1.5}Te_3$, and (e and f) Sb_2Te_3 thick films as a function of curing temperature. All samples are cured for 6 h.

combinations are $Bi_2Te_{2.7}Se_{0.3}$. The p-type legs are $Bi_{0.5}Sb_{1.5}Te_3$ and Sb_2Te_3. The output power is caused by the differences of the internal resistance between two combinations ($Bi_2Te_{2.7}Se_{0.3}$–$Bi_{0.5}Sb_{1.5}Te_3$ ~ 5951 Ω, $Bi_2Te_{2.7}Se_{0.3}$–Sb_2Te_3 ~ 191.13 Ω). The results of the test have confirmed the characterization of the material. The combined open-circuit voltage of the $Bi_{0.5}Sb_{1.5}Te_3$ case is 15.84% higher than that of the Sb_2Te_3 because of the slightly higher Seebeck coefficient (Table 2). Although its Seebeck coefficient of p-type $Bi_{0.5}Sb_{1.5}Te_3$ is high, its intrinsic resistivity is higher than the other. The output power of the $Bi_{0.5}Sb_{1.5}Te_3$ scheme is lower than that of the Sb_2Te_3 scheme with an order of magnitude. The $Bi_2Te_{2.7}Se_{0.3}$–Sb_2Te_3 scheme exhibits an excellent comprehensive performance. The results show that compared to $Bi_{0.5}Sb_{1.5}Te_3$,

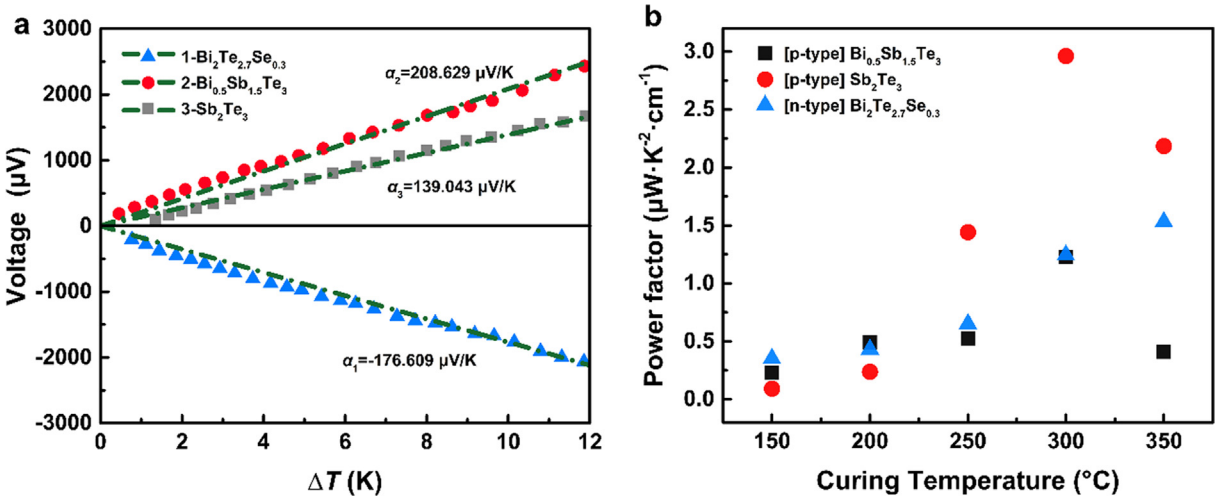

Fig. 4. (a) Seebeck coefficient. (b) Power factor.

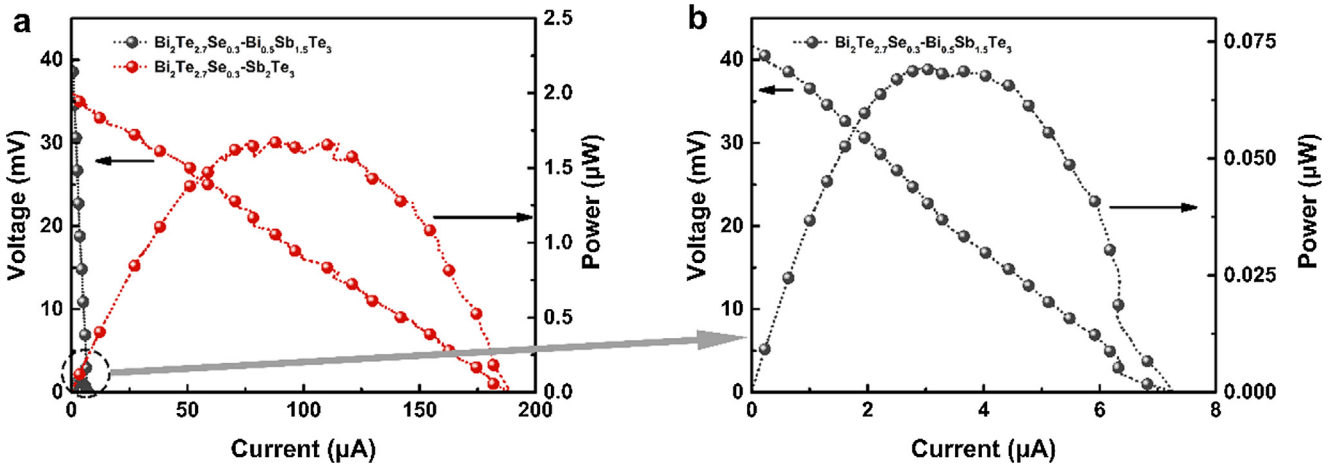

Fig. 5. Output performance of two TE leg devices loaded with 0.75 W thermal power.

Sb_2Te_3 is more suitable for MRTG. The conductive epoxy silver is not used as connection electrode, but the TE material itself is connected to the electrode to avoid the catalyst poisoning effect in this experiment.

3.3. Output performance of MRTG

$$V_{oc} = N\cdot(\alpha_p - \alpha_n)\cdot\Delta T \tag{7}$$

The maximum power P_{max} is obtained through matching the external load and the internal resistance of the generator, i.e., $R_{load} = R_{int}$, and it is related to V_{oc}, as shown in the following equation:

$$P_{max} = \frac{V_{oc}^2}{4R_{int}} \tag{8}$$

Fig. 7d shows the output performance of the calculated values of thermal power and electrical output and a comparison with the experimental measuring values of Table 2.

The internal resistance of a typical prototype MRTG is shown in Fig. 7a, and the slope of *I–V* is approximately 191.14 Ω. Good linearity is maintained in the wide range of voltage current, and the stability of resistance enables a stable output of power generation. After loading 0.125–1.5 W heat source, the temperature of cold and hot ends increases along with the increased heat source power. The ΔT of TE leg also increases with the increased power. MRTG resistance still keeps stable amid various heat source power, with only 3.1 Ω (3.30%) increased within 0–1 W and 13.68 Ω (7.04%) increased within 1–1.5 W.

The current–voltage–power curves (Fig. 7c) of the MRTG are obtained through changing the radioisotope heat source power (thermal power) of five couples of TE legs ($Bi_2Te_{2.7}Se_{0.3}$–Sb_2Te_3 ~ 191.13 Ω) from 0.125 W to 1.5 W (ΔT is 3.6 °C to 48.3 °C).

The maximum thermal power from various isotope heat source pellets with the same volume of heat source is shown in Fig. 7d. As the thermal power function of the MRTG, the open-circuit voltage, short-circuit current, and maximum power are shown as well. The relationship between heat source power and ΔT presents an approximate linear, thereby causes the output voltage and output power to increase linearly and quadratically respectively, along with the thermal power.

When the heat source power value is within 0.125–1.5 W, the output open-circuit voltage ranges from 6.61 mV to 68.41 mV, the short-circuit current ranges from 34.56 μA to 329.0 μA, and the maximum output power ranges from 54.47 nW to 5.81 μW. The maximum output performance of three radioisotope heat sources is shown in Table 3. Compared with the non-optimized materials and process in the past, the improvement of output performance is apparent. The optimization process is essential for this kind of micro-power supply, which will directly affect the quality of the power supply. The functions of extrapolation and interpolation data are shown in Table S5. The prototype power density in this work is 237.7 μW cm^{-3}, which forms an upgrade of 128.5% over that of similar devices [9]. The research results show that the output power density of monolithic radioisotope thermoelectric generators increases significantly. This result has positive

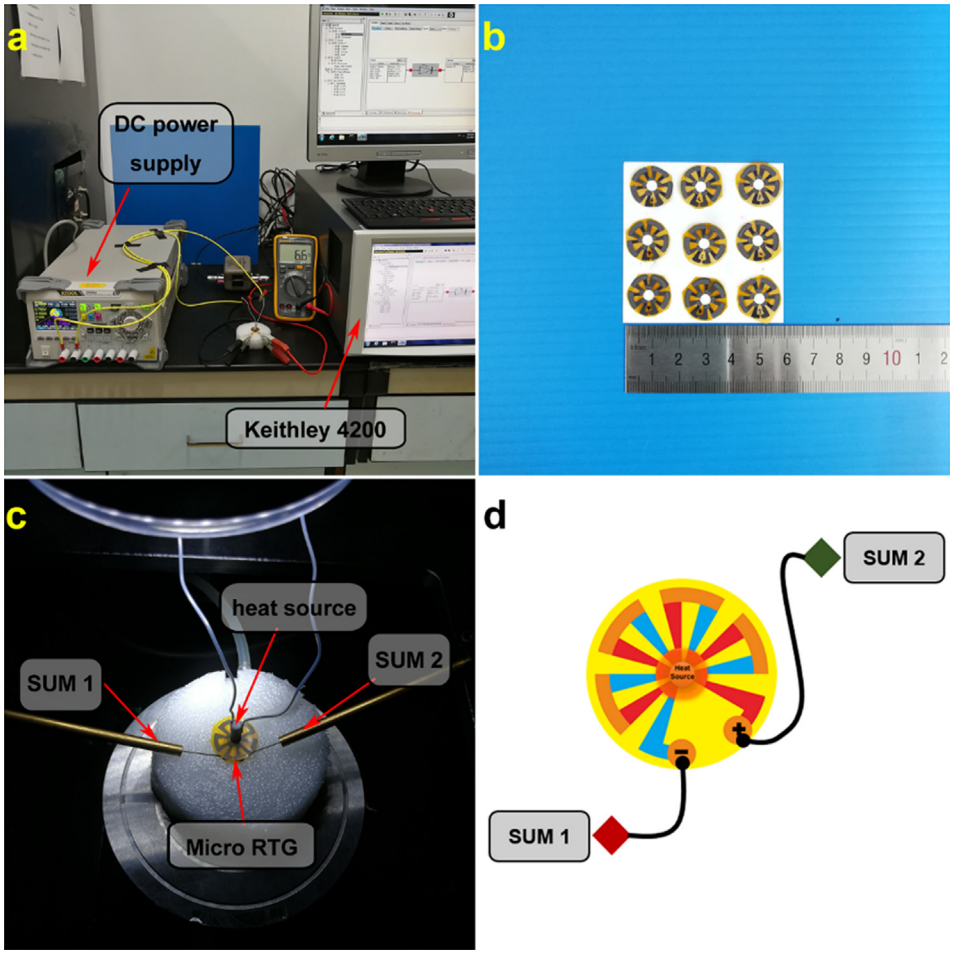

Fig. 6. (a, b, and d) Electrical output measurement of prototype device. (c) Prototype size.

Table 2
Material properties of printed thermoelectric/epoxy composites measured at room temperature.

Composite material	α ($\mu V \cdot K^{-1}$)	σ ($S \cdot cm^{-1}$)	$\alpha^2\sigma$ ($W \cdot m^{-1} \cdot K^{-2}$)	μ ($cm^2 \cdot V^{-1} \cdot s^{-1}$)	n (cm^{-3})
n-type $Bi_2Te_{2.7}Se_{0.3}$	−176.6	39.89	1.24×10^{-4}	29.63	-1.15×10^{19}
p-type $Bi_{0.5}Sb_{1.5}Te_3$	223.3	24.57	1.23×10^{-4}	27.34	1.91×10^{19}
p-type Sb_2Te_3	139.7	165.8	3.21×10^{-4}	54.41	5.85×10^{18}

significance for the development of device stacking and series-paralleling. According to the specific application of MEMS, the prototypes of this paper are stacked and connected in parallel to obtain a suitable power and voltage range. In real practice, they can provide ultra-low power MEMS of space detectors, such as accelerometers and wireless sensor networks with electricity. The typical micro-power three-axis accelerometer MEMS (ADXL372) requires 22 μA of current and 2.5 V of voltage. The $^{238}PuO_2$ prototype stacked in series requires 36 layers to drive the MEMS. Our research team is conducting multilayer prototype research and manufacture work.

4. Conclusions

In this work, we have developed the relatively low-temperature curing epoxy resin matrix composite thermoelectric material used for micro radioisotope thermoelectric generators, and have further improved the preparation process and optimized the curing temperature. Based on the experimental results of the material properties, the curing temperature of 300 °C and molding process with two curing steps are preferred. We have also found that Sb_2Te_3 is more suitable for the resin thermoelectric composite material system compared to $Bi_{0.5}Sb_{1.5}Te_3$. Furthermore, we have made the radial structure micro radioisotope thermoelectric generator prototype devices by screen printing. Given the optimization of the Seebeck coefficient power factor and the internal resistance, the performance of the device is significantly better than that of the previous micro radioisotope thermoelectric generator. The p-type and n-type thermoelectric legs printed on a 75 μm polyimide have electrical conductivity of approximately 165.8 and 39.89 S cm^{-1}, with Seebeck coefficients of 139.7 and $-176.6\ \mu V\ K^{-1}$ respectively. Loaded with a $^{238}PuO_2$ radioisotope heat source, the prototype of the five-pair thermoelectric legs supplies the maximum output power of 6.31 μW at 35.66 mV, the short-circuit current of 356.6 μA, open-voltage of 71.82 mV, and power density of 237.7 μW cm^{-3}, and the calculation results are consistent with the experimental results. The electrical output of the multilayer prototype is expected to drive some μA-level sensors and actuators. In the future, we will improve the efficiency by making planar array and space stack thermoelectric devices.

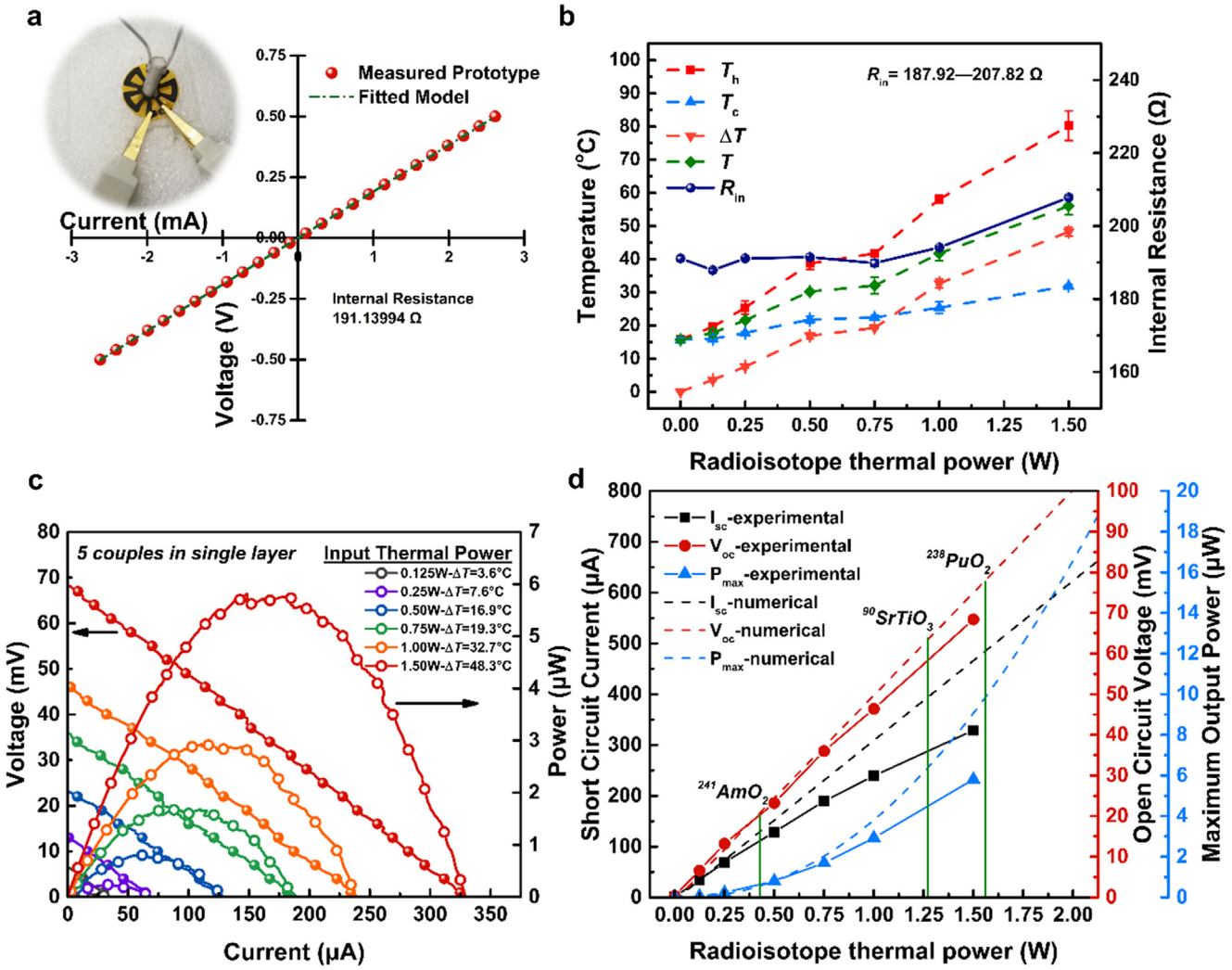

Fig. 7. Electrical performance of prototype. (a) Internal resistance. (b) Relationship between thermal power of radioisotope and internal resistance of system temperature. (c and d) Relationship between thermal power of radioisotope and electrical output of device.

Table 3
Output performance comparison of prototype [13].

Test	P_{th}	I_{sc}	V_{oc}	P_{max}
Ideal	0.5 W	1.98 mA	46.73 mV	23.13 μW at 23.37 mV
Previous	0.5 W	3.52 μA	14.26 mV	12.57 nW at 7.51 mV
This work	$^{241}AmO_2$ = 0.431 W	10.67 μA	20.58 mV	0.67 μW at 11.35 mV
	$^{90}SrTiO_3$ = 1.287 W	295.3 μA	59.29 mV	4.43 μW at 29.82 mV
	$^{238}PuO_2$ = 1.564 W	356.6 μA	71.82 mV	6.31 μW at 35.66 mV

Acknowledgements

This work is supported by the National Natural Science Foundation of China (Grant Nos. 11675076, 11505096); the Jiangsu Planned Projects for Postdoctoral Research Funds (Grant No. 1601139B); the Funding of Jiangsu Innovation Program for Graduate Education (Grant No. KYLX16_0355); the Shanghai Aerospace Science and Technology Innovation Project (Grant No. SAST2016112); and the Priority Academic Program Development of Jiangsu Higher Education Institutions.

Appendix A. Supplementary material

Supplementary data associated with this article can be found, in the online version, at http://dx.doi.org/10.1016/j.apenergy.2018.05.073.

References

[1] Prelas M, Boraas M, De La Torre Aguilar F, Seelig JD, Tchakoua Tchouaso M, Wisniewski D. Nuclear batteries and radioisotopes, vol. 56; 2016. 10.1007/978-3-319-41724-0.
[2] Prelas MA, Weaver CL, Watermann ML, Lukosi ED, Schott RJ, Wisniewski DA. A review of nuclear batteries. Prog Nucl Energy 2014;75:117–48. http://dx.doi.org/10.1016/j.pnucene.2014.04.007.
[3] Rowe DM. Applications of nuclear-powered thermoelectric generators in space. Appl Energy 1991;40:241–71. http://dx.doi.org/10.1016/0306-2619(91)90020-X.
[4] Heshmatpour B, Lieberman A, Khayat M, Leanna A, Dobry T, El-Genk MS. Special application thermoelectric micro isotope power sources. AIP conf proc, vol. 969, AIP; 2008. p. 689–95. 10.1063/1.2845032.
[5] Roundy S, Steingart D, Frechette L, Wright P, Rabaey J. Power sources for wireless sensor networks. Sens Netw 2004;2920:1–17. http://dx.doi.org/10.1007/978-3-540-24606-0_1.
[6] Yan J, Liao X, Yan D, Chen Y. Review of micro thermoelectric generator. J Microelectromech Syst 2018;27:1–18. http://dx.doi.org/10.1109/JMEMS.2017.

2782748.
[7] Wang Y, Shi Y, Mei D, Chen Z. Wearable thermoelectric generator to harvest body heat for powering a miniaturized accelerometer. Appl Energy 2018;215:690–8. http://dx.doi.org/10.1016/j.apenergy.2018.02.062.
[8] Kim CS, Lee GS, Choi H, Kim YJ, Yang HM, Lim SH, et al. Structural design of a flexible thermoelectric power generator for wearable applications. Appl Energy 2018;214:131–8. http://dx.doi.org/10.1016/j.apenergy.2018.01.074.
[9] Whalen SA, Apblett CA, Aselage TL. Improving power density and efficiency of miniature radioisotopic thermoelectric generators. J Power Sour 2008;180:657–63. http://dx.doi.org/10.1016/j.jpowsour.2008.01.080.
[10] Menon AK, Meek O, Eng AJ, Yee SK. Radial thermoelectric generator fabricated from n- and p-type conducting polymers. J Appl Polym Sci 2017;134. http://dx.doi.org/10.1002/app.44060.
[11] Menon AK, Yee SK. Design of a polymer thermoelectric generator using radial architecture. J Appl Phys 2016;119. http://dx.doi.org/10.1063/1.4941101.
[12] Liu K, Liu Y, Xu Z, Zhang Z, Yuan Z, Guo X, et al. Experimental prototype and simulation optimization of micro-radial milliwatt-power radioisotope thermoelectric generator. Appl Therm Eng 2017;125:425–31. http://dx.doi.org/10.1016/j.applthermaleng.2017.07.022.
[13] Yuan Z, Tang X, Liu Y, Xu Z, Liu K, Zhang Z, et al. A stacked and miniaturized radioisotope thermoelectric generator by screen printing. Sens Actuators A Phys 2017;267:496–504. http://dx.doi.org/10.1016/j.sna.2017.10.055.
[14] Russo V, Bailini A, Zamboni M, Passoni M, Conti C, Casari CS, et al. Raman spectroscopy of Bi-Te thin films. J Raman Spectrosc 2008;39:205–10. http://dx.doi.org/10.1002/jrs.1874.
[15] Kim SJ, We JH, Cho BJ. [15] A wearable thermoelectric generator fabricated on a glass fabric. Energy Environ Sci 2014;7:1959. http://dx.doi.org/10.1039/c4ee00242c.
[16] We JH, Kim SJ, Cho BJ. Hybrid composite of screen-printed inorganic thermoelectric film and organic conducting polymer for flexible thermoelectric power generator. Energy 2014;73:506–12. http://dx.doi.org/10.1016/j.energy.2014.06.047.
[17] Kim F, Kwon B, Eom Y, Lee JE, Park S, Jo S, et al. 3D printing of shape-conformable thermoelectric materials using all-inorganic Bi2Te3-based inks. Nat Energy 2018. http://dx.doi.org/10.1038/s41560-017-0071-2.
[18] Park SH, Jo S, Kwon B, Kim F, Ban HW, Lee JE, et al. High-performance shape-engineerable thermoelectric painting. Nat Commun 2016;7. http://dx.doi.org/10.1038/ncomms13403.
[19] Varghese T, Hollar C, Richardson J, Kempf N, Han C, Gamarachchi P, et al. High-performance and flexible thermoelectric films by screen printing solution-processed nanoplate crystals. Sci Rep 2016;6. http://dx.doi.org/10.1038/srep33135.
[20] Jung YS, Jeong DH, Kang SB, Kim F, Jeong MH, Lee KS, et al. Wearable solar thermoelectric generator driven by unprecedentedly high temperature difference. Nano Energy 2017;40:663–72. http://dx.doi.org/10.1016/j.nanoen.2017.08.061.
[21] Hyland M, Hunter H, Liu J, Veety E, Vashaee D. Wearable thermoelectric generators for human body heat harvesting. Appl Energy 2016;182:518–24. http://dx.doi.org/10.1016/j.apenergy.2016.08.150.
[22] Lu Z, Zhang H, Mao C, Li CM. Silk fabric-based wearable thermoelectric generator for energy harvesting from the human body. Appl Energy 2016;164:57–63. http://dx.doi.org/10.1016/j.apenergy.2015.11.038.
[23] Siddique ARM, Mahmud S, Van Heyst B. A review of the state of the science on wearable thermoelectric power generators (TEGs) and their existing challenges. Renew Sustain Energy Rev 2017;73:730–44. http://dx.doi.org/10.1016/j.rser.2017.01.177.
[24] Madan D, Wang Z, Wright PK, Evans JW. Printed flexible thermoelectric generators for use on low levels of waste heat. Appl Energy 2015;156:587–92. http://dx.doi.org/10.1016/j.apenergy.2015.07.066.
[25] Gima ZT, Gururangan K, Evans J, Wright P. Annular screen printed thermoelectric generators for ultra-low-power sensor applications. J Phys: Conf Ser 2016;773. http://dx.doi.org/10.1088/1742-6596/773/1/012115.
[26] Iezzi B, Ankireddy K, Twiddy J, Losego MD, Jur JS. Printed, metallic thermoelectric generators integrated with pipe insulation for powering wireless sensors. Appl Energy 2017;208:758–65. http://dx.doi.org/10.1016/j.apenergy.2017.09.073.
[27] Cheon SJ, Hong SG, Lee JH, Nam YS. Design and performance analysis of a 500-W heat source for radioisotope thermophotovoltaic converters. Int J Energy Res 2017:1–13. http://dx.doi.org/10.1002/er.3889.
[28] Madan D, Wang Z, Chen A, Wright PK, Evans JW. High-performance dispenser printed MA p-type Bi0.5Sb 1.5Te3 flexible thermoelectric generators for powering wireless sensor networks. ACS Appl Mater Interf 2013;5:11872–6. http://dx.doi.org/10.1021/am403568t.
[29] Madan D, Wang Z, Chen A, Juang RC, Keist J, Wright PK, et al. Enhanced performance of dispenser printed MA n-type Bi2Te3composite thermoelectric generators. ACS Appl Mater Interf 2012;4:6117–24. http://dx.doi.org/10.1021/am301759a.
[30] Choi H, Kim SJ, Kim Y, We JH, Oh M-W, Cho BJ. Enhanced thermoelectric properties of screen-printed Bi0.5Sb1.5Te3 and Bi2Te2.7Se0.3 thick films using a post annealing process with mechanical pressure. J Mater Chem C 2017. http://dx.doi.org/10.1039/C7TC01797A.
[31] Cao Z, Tudor MJ, Torah RN, Beeby SP. Screen printable flexible BiTe-SbTe-based composite thermoelectric materials on textiles for wearable applications. IEEE Trans Electron Dev 2016;63:4024–30. http://dx.doi.org/10.1109/TED.2016.2603071.
[32] Madan D, Chen A, Wright PK, Evans JW. Dispenser printed composite thermoelectric thick films for thermoelectric generator applications. J Appl Phys 2011;109. http://dx.doi.org/10.1063/1.3544501.